Doping Strategy for Manganese-Based Zinc-ion Battery Cathode

Subjects: Electrochemistry | Nanoscience & Nanotechnology

Contributor: Bomian Zhang , Jinghui Chen , Weiyi Sun , Yubo Shao , Lei Zhang , Kangning Zhao

As one of the most appealing options for large-scale energy storage systems, the commercialization of aqueous zinc-ion batteries (AZIBs) has received considerable attention due to their cost effectiveness and inherent safety. A potential cathode material for the commercialization of AZIBs is the manganese-based cathode, but it suffers from poor cycle stability, owing to the Jahn–Teller effect, which leads to the dissolution of Mn in the electrolyte, as well as low electron/ion conductivity. In order to solve these problems, various strategies have been adopted to improve the stability of manganese-based cathode materials.

zinc-ion battery | manganese-based oxides | ion doping | Mn dissolution | zinc–manganese battery

1. Introduction

Due to the excessive consumption of fossil fuels and the growing problem of climate change caused by environmental pollution, renewable energy research and development, such as solar, wind, and tidal energy, has attracted worldwide attention [1][2][3][4]. However, renewable energy power generation is often intermittent and unpredictable, which requires large-scale energy storage systems to effectively buffer such fluctuations to achieve stable energy output for smart grid [5][6][7]. As an efficient and flexible energy storage device, lithium-ion batteries (LIBs) have not only been successfully applied in electronic consumer products such as cellphones and laptops, but are also expanding their range to electric vehicles and other fields [8][9][10][11]. However, the high production cost, limited lithium resource reserves, and the use of toxic and flammable organic electrolytes make lithium-ion batteries expensive, hazardous, and environmentally polluting, strongly impeding their further development and application in grid-scale energy storage [12][13][14]. Therefore, researchers are seeking new energy storage battery systems to replace LIBs in terms of cost, safety, and sustainability.

Among those energy storage devices, aqueous electrolytes have been widely employed in secondary battery systems for Na, K, Mg^{++2+}, Al^{3+}, Ca^{2+}, Zn^{2+}, etc. in recent years because of their safety, high ionic conductivity, and ease of operation [15][16]. Among aqueous multivalent ion batteries, ZIBs stand out due to the following characteristics: (1) Zn metal reserves are abundant and the manufacture process of ZIBs occurs in an air environment, making it cost-effective; (2) Zn metal anode has a low redox potential of −0.76 V with respect to a standard hydrogen electrode and high theoretical gravimetric/volumetric capacity (820 $mAh{\cdot}g^{-1}$/5855 $mAh{\cdot}cm^{-3}$); (3) Zn metal can be directly applied as an anode due to its excellent electrochemical stability and reversibility in water; (4) ZIBs are highly safe because of the application of nontoxic aqueous electrolyte [17][18]. However, considering the large ionic radius of hydrated zinc (5.5 Å vs. 0.74 Å for Zn ion), the intercalation of hydrated zinc ions would either require large spacing to accommodate the large ions or withstand a large desolvation penalty for smaller dehydrated ions to intercalate, imposing a great challenge in the development of suitable cathode materials [19]. At present, manganese-based oxides, vanadium-based oxides, and Prussian blue analogs are mainly developed as cathode materials for ZIBs [20]. Among them, manganese-based oxides are widely recognized as candidates for the commercialization of ZIBs because of their mature synthesis process, abundant resources, lack of pollution, high specific capacity, and high operating voltage [21]. However, the further application of Mn-based cathodes is hindered by two major issues. The redox reaction involving Mn^{4+} is usually accompanied by the Jahn–Teller effect and leads to the formation of Mn^{2+}, which tends to dissolve into the electrolyte and lead to irreversible capacity loss. On the other hand, the poor ion/electric conductivity of the transition metal oxide would sacrifice the rate capability of the zinc battery [9][22][23]. At present, various strategies such as nanostructure engineering [24][25][26], conductive agent coating [27], and ion doping are widely adopted to tackle the above problems [21][28][29]. Among the various strategies, ion doping involves a small number of guest ions being preinserted into the manganese-based oxide framework and interacting with the host atoms to achieve an inherent structure optimization, which significantly enhances the electrochemical performance from a fundamental thermodynamics and dynamics aspect. This approach is recognized as an efficient and straightforward optimization strategy, breaking through the limitations of the inherent crystallographic structure [30].

2. Synthesis Strategy for Ion-Doped Manganese-Based Oxides

Manganese oxides are highly dependent on dopant ions due to their effect on the crystalline phase, crystal structure, and average valence of the manganese oxides [31][32][33]. Daniil et al. built an ab initio model using the SCAN function to reveal the effect of doping different guest ions on the formation of manganese dioxide with different phases, as depicted in **Figure 1**a [31]. As shown in **Figure 1**b, the doping of Na, K, and Ca^{++2+} was more likely to form α-MnO_2, whereas Li and Mg^{+2+} favored the formation of γ-MnO_2, and δ-MnO_2 was easily stabilized by Na. The mechanistic basis was that distinct metal ion doping resulted in varied formation free energies required for the different phases of manganese dioxide. Hu et al. demonstrated that partial Mg^{+2+} intercalation resulted in tunnels of various sizes, such as 3 × 3, 4 × 3, and 5 × 3 tunnels in T-MnO_2, not just 3 × 3 tunnels [32]. Furthermore, the synthesis methods and synthesis circumstances also have a significant impact on the electrochemical performance of manganese oxides. Up to now, various synthesis methods have been widely applied in ion doping, including the hydrothermal method, ion penetration/exchange method, electrodeposition method, and calcination treatment.

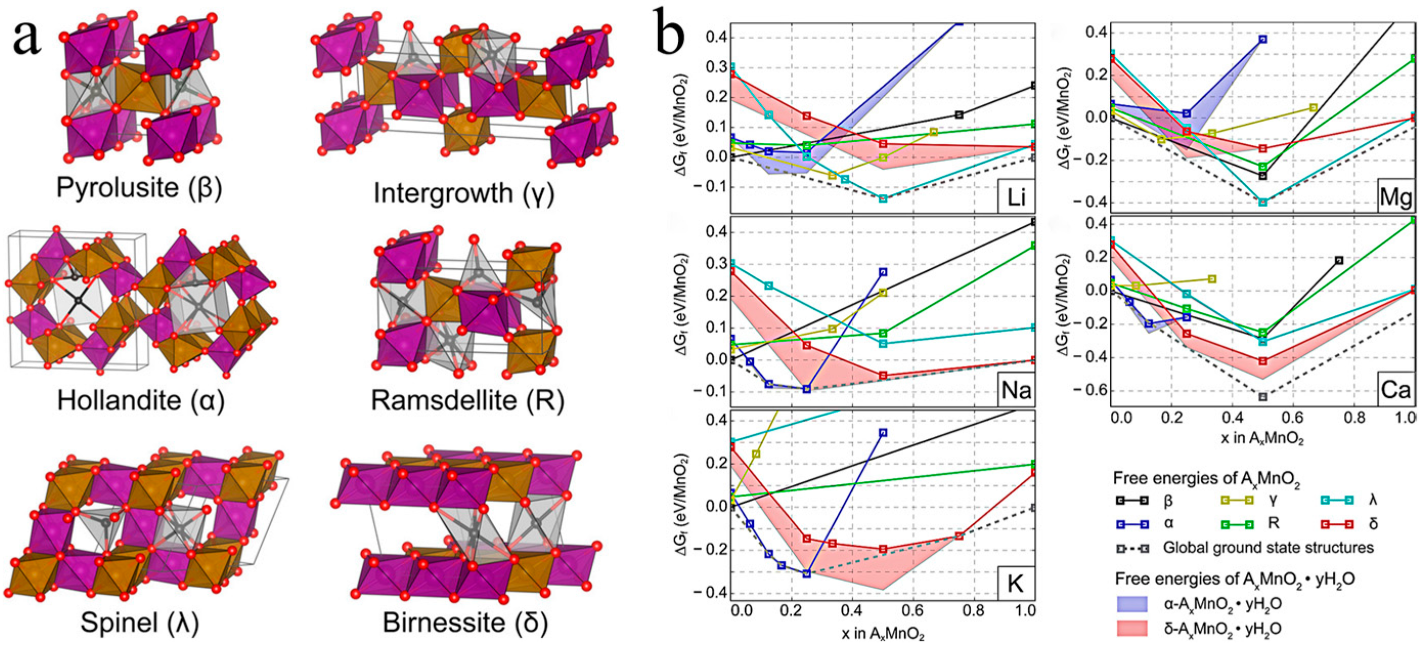

Figure 1. (**a**) Crystal structures of various manganese-based oxides [31]. (**b**) The formation free energies for $A_xMnO_2{\cdot}H_2O$ when doping with Li, Na, K, Mg^{+++2+}, and Ca^{2+} [31].

2.1. Hydrothermal Method

Because of its simple controllability over the diverse crystal phases of manganese-based oxides, hydrothermal synthesis is the most frequently used approach for ion doping. Ion doping can be controlled by the addition of the different ions in the raw solutions before hydrothermal treatment. Zhang et al. prepared α-$K_{0.19}MnO_2$ nanotubes via decomposition of $KMnO_4$ combined with carbon nanofibers as templates in 2019 [34]. Under the hydrothermal conditions of 140 °C for 10 h, a typical K-doped tunnel structure was achieved. The reaction mechanism was as follows: K + $MnO^{++}{}_4^-$ + C + H_2O → δ-$K_{0.19}MnO_2{\cdot}nH_2O$ + CO_3^{2-} + HCO_3^-. Through a similar route, $MnO_2H_{0.16}(H_2O)_{0.27}$ nanolayers were synthesized via the reaction of $KMnO_4$ with acetylene black at 120 °C for 24 h by Pan et al. [35]. Interestingly, this new phase exhibited excellent rate capability (115.1 mAh·g^{-1} at 10 °C) with robust structural stability even with an interlayer spacing of less than 0.3 nm. Moreover, they developed a layered $K_{0.36}H_{0.26}MnO_2{\cdot}0.28H_2O$ via the neutralization reaction of $KMnO_4$ and $MnSO_4$ with K_2SO_4 additive as an excellent cathode in ZIBs [36]. The layer-type structure of monoclinic birnessite phase was obtained following a hydrothermal reaction of 120 °C for 12 h with a large interlayer spacing (7.12 Å). Shi et al. synthesized a cathode ($K_{0.29}MnO_2{\cdot}0.67H_2O$) with a larger interplanar spacing (7.4 Å) through a hydrothermal potassium insertion strategy [37]. Peng et al. developed a Na-incorporated layered δ-$MnO^{+}{}_2$ by subjecting K-containing δ-$MnO^{+}{}_2$ to hydrothermal treatment using a 0.5 mol·L^{-1} Na_2SO_4 solution at 180 °C for 3 h [38]. Layered $Ca_{0.28}MnO_2{\cdot}0.5H_2O$ was synthesized by Tao et al. through a hydrothermal method at 160 °C for 12 h using $CaCl_2$, $KMnO_4$, and $MnSO_4$ as reactants with a molar ratio of 1:6:1 [39]. This work demonstrated that divalent alkaline earth metal ions could also support layered manganese oxides, resulting in excellent electrochemical performance. Li et al. successfully incorporated Ni^{2+} into α-MnO_2 for boosting the diffusion kinetics of protons in the tunnels, which proved the substitution of divalent metal ions for Mn sites in tunnel-type manganese based oxides [40]. Du et al. found that the addition of Ce^{3+} ions during hydrothermal synthesis could induce a phase transition of MnO_2 from β to α, which resulted in a larger tunnel structure (2.3 × 2.3 $Å^2$ vs. 4.6 × 4.6 $Å^2$) [41]. Wang et al. developed a Bi^{3+}-doped α-MnO_2 cathode with an enlarged lattice spacing [42]. First, $Bi(NO_3)_3$ and $MnSO_4$ were mixed uniformly; then, $KMnO_4$ was added and stirred for 2 h, before being transferred to a 100 mL autoclave and reacting at 120 °C for 12 h. Yan at al. also designed Al-intercalated α-MnO_2 using a hydrothermal approach with a narrower electronic bandgap [43]. Interestingly, Al-doped MnO_2 exhibited a sea urchin-like morphology with a size of 4.5–5.0 µm and an enlarged interlayer spacing (0.24 nm vs. 0.29 nm). Xiong et al. reported that Al-doped α-MnO_2 coated with lignin was formed through a hydrothermal reaction involving $KMnO_4$, NH_4F, $Al_2(SO_4)_3$, and lignosulfonate at 200 °C, as illustrated in **Figure 2**a [44].

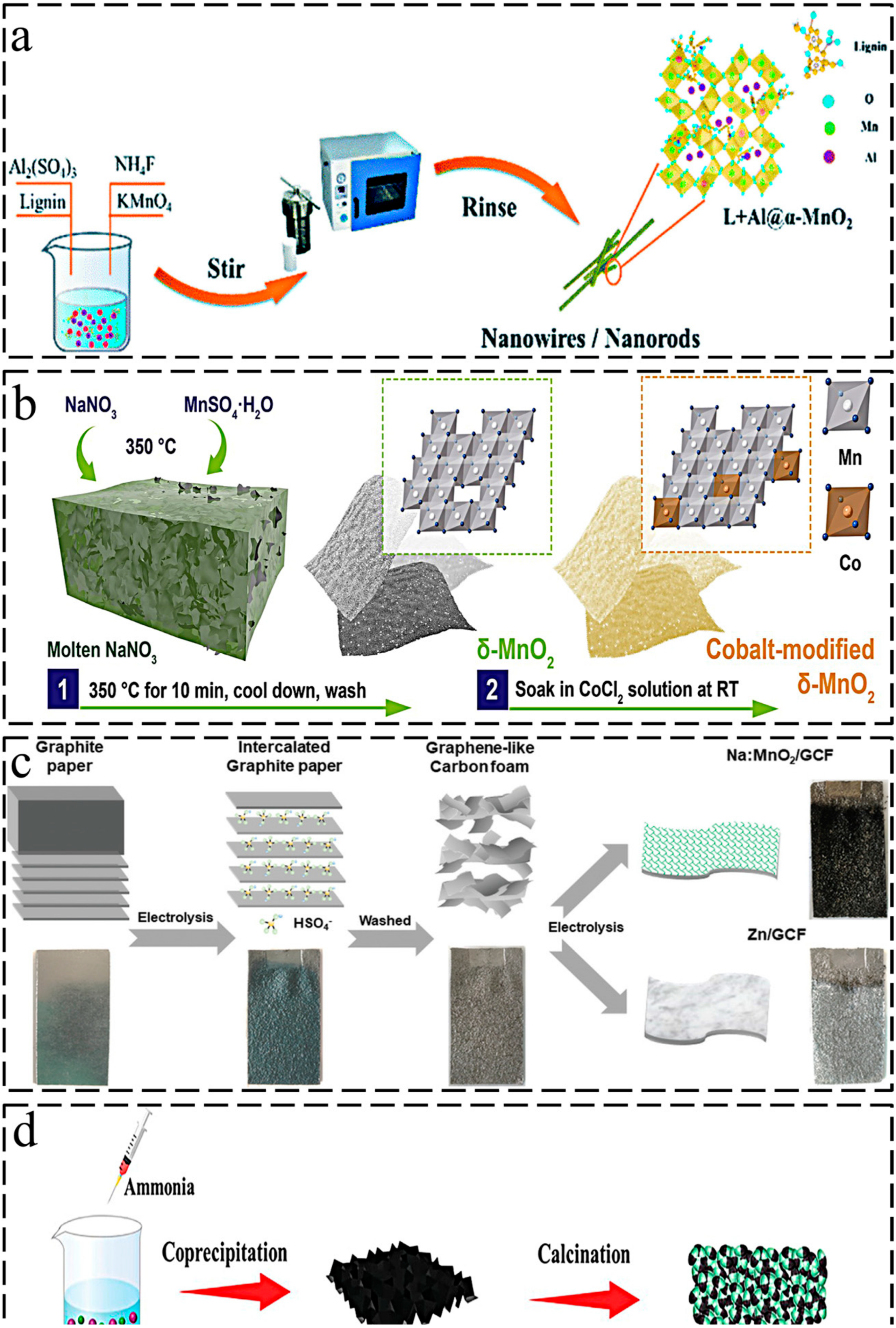
a
$Al_2(SO_4)_3$
Lignin
NH_4F
$KMnO_4$
Stir
Rinse
Lignin
O
Mn
Al
L+Al@α-MnO_2
Nanowires / Nanorods
b
$NaNO_3$
$MnSO_4 \cdot H_2O$
350 °C
Molten $NaNO_3$
δ-MnO_2
Mn
Co
Cobalt-modified δ-MnO_2
1 350 °C for 10 min, cool down, wash
2 Soak in $CoCl_2$ solution at RT
c
Graphite paper
Intercalated Graphite paper
Graphene-like Carbon foam
Na:MnO_2/GCF
Electrolysis
HSO_4^-
Washed
Electrolysis
Zn/GCF
d
Ammonia
Coprecipitation
Calcination

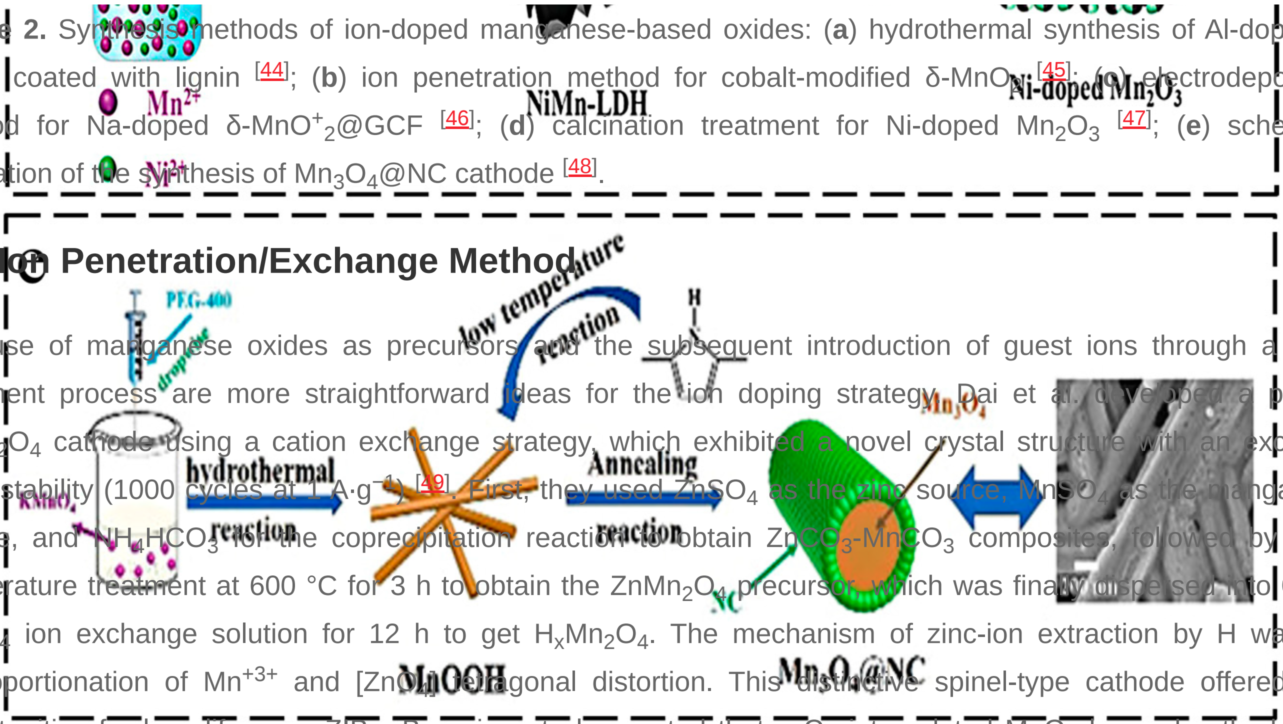

Figure 2. Synthesis methods of ion-doped manganese-based oxides: (**a**) hydrothermal synthesis of Al-doped α-MnO_2 coated with lignin [44]; (**b**) ion penetration method for cobalt-modified δ-MnO_2 [45]; (**c**) electrodeposition method for Na-doped δ-$MnO^+{}_2$@GCF [46]; (**d**) calcination treatment for Ni-doped Mn_2O_3 [47]; (**e**) schematic illustration of the synthesis of Mn_3O_4@NC cathode [48].

2.2. Ion Penetration/Exchange Method

The use of manganese oxides as precursors and the subsequent introduction of guest ions through a post-treatment process are more straightforward ideas for the ion doping strategy. Dai et al. developed a porous $H_xMn_2O_4$ cathode using a cation exchange strategy, which exhibited a novel crystal structure with an excellent cycle stability (1000 cycles at 1 A·g^{-1}) [49]. First, they used $ZnSO_4$ as the zinc source, $MnSO_4$ as the manganese source, and NH_4HCO_3 for the coprecipitation reaction to obtain $ZnCO_3$-$MnCO_3$ composites, followed by high-temperature treatment at 600 °C for 3 h to obtain the $ZnMn_2O_4$ precursor, which was finally dispersed into 0.5 M H_2SO_4 ion exchange solution for 12 h to get $H_xMn_2O_4$. The mechanism of zinc-ion extraction by H was the disproportionation of Mn^{+3+} and [ZnO_4] tetragonal distortion. This distinctive spinel-type cathode offered new opportunities for long-life span ZIBs. Banerjee et al. reported that a Cu-intercalated MnO_2 layered cathode was attained by mixing the prepared MnO_2 powder with a 1 M $CuSO_4$ solution for 48 h [50]. The penetration of Cu^{2+} into δ-MnO_2 resulted in an enlarged lattice spacing, thereby lowering the charge transfer resistance. Furthermore, they exploited the redox potential of Cu for full capacity using two electrons. A cobalt-modified δ-MnO_2 with a redox-active surface showed superior self-recovery capability, as reported by Shao et al. [45]. As shown in **Figure 2**b, a molten-salt method was adopted to synthesize δ-MnO_2 using $MnSO_4·H_2O$ and $NaNO_3$ as the reactants, and then δ-MnO_2 powder was mixed with 1 M $CoCl_2$ aqueous solution by constant stirring for 8 h at room temperature. The deposition–dissolution mechanism was proven by the electrochemical performance (over 500 mAh·g^{-1}), and Co^{2+} played a catalytic role in the electrochemical deposition of Mn^{2+}. In addition, a Mn^{2+} additive was introduced into the electrolyte for enhanced cycle-stability.

2.3. Electrodeposition Method

Electrodeposition methods often involve depositing an electrolyte onto a conductive substrate by applying a certain current or voltage, which has the advantage of outstanding conductivity because of the highly conductive substrate. Dai et al. prepared a Na-doped $MnO^+{}_2$@GCF cathode via the electrodeposition of 0.1 M Na_2SO_4 and 0.05 M $MnSO_4·H_2O$ onto a graphene-like carbon film (GCF) [46]. The cathode was synthesized through a two-step procedure. As illustrated in **Figure 2**c, they first transformed the raw graphite paper into GCF by electrodepositing it into H_2SO_4 electrolyte, which had a 2D–3D hybrid network composed of graphene sheets. Then, the H_2SO_4 electrolyte was replaced by $NaSO_4$ and $MnSO_4·H_2O$ to obtain Na-doped $MnO^+{}_2$@GCF. The prepared cathode achieved excellent energy density (511.9 Wh·kg^{-1} at 137 W·kg^{-1}). A Co–MnO_2 membrane was electrodeposited onto N-decorated carbon cloth (N-CC) by Nakayama et al. [51] in 2020, using an electrolyte consisting of $MnSO_4$, $ZnSO_4$, and $CoSO_4$. Furthermore, the cathode delivered an impressive capacity of 280 mAh·g^{-1}, even at 1.2 A·g^{-1}. Wang et al. reported the electrodeposition synthesis of multivalence cobalt-doped Mn_3O_4 (Co-Mn_3O_4) [52]. Similarly, a pretreated carbon cloth was applied as the substrate, while the cobalt and manganese sources were $Co(CH_3COO)_2{\cdot}4H_2O$ and $Mn(CH_3COO)_2{\cdot}4H_2O$, respectively. Moreover, cobalt was present in multiple valence forms in the manganese oxides and played different roles, resulting in improved charge/ion transport and enhanced structure stability.

2.4. Calcination Treatment

Calcination treatment can provide high kinetics for guest ion intercalation, which is also applicable for manganese-based oxide doping strategies. Low-bandgap $Ni_xMn_{3-x}O_4$ nanoparticles were synthesized by Guo et al. through different calcination processes using manganese acetate as the manganese source and nickel acetate as the additive [53]. A Ni–Mn-layered double hydroxide-derived Ni-doped Mn_2O_3 (NM) was developed by Huang et al. [47]. First, the precursor Ni–Mn-LDH was formed by adding ammonia to a mixture of $Ni(NO_3)_2{\cdot}6H_2O$, $MnSO_4{\cdot}H_2O$, and NH_4F for coprecipitation at room temperature, and then Ni-doped Mn_2O_3 was obtained by calcining the precursor at 450 °C, as depicted in **Figure 2**d. A metal–organic framework template strategy was adopted by Sun et al. to synthesize a N-doped Mn-based cathode (MnO_x@N-C) [54]. Firstly, MnO_2 was generated by decomposing potassium permanganate under an acidic environment, and then MnO_2 was mixed with PVP, $Zn(NO_3)_2{\cdot}6H_2O$, and 2-methylimidazole at room temperature to produce PVP-modified MnO_2@ZIF-8. Finally, MnO_x@N-C was obtained via calcination of MnO_2@ZIF-8 at 700 °C. Xia et al. fabricated a N-doped MnO_{2-x} cathode by calcining MnO_2 at 200 °C under an NH_3 atmosphere [55]. MnO_2 was deposited on TiC/C via $KMnO_4$ decomposition, while N doping was processed by NH_3 treatment at low temperature. Li et al. designed a N-doped $Na_2Mn_3O_7$ (N-NMO) in combination with sodium pre-intercalation and nitrification strategies [56]. In the first step, they used a chemical reaction involving $KMnO_4$, $C_6H_{12}O_6$, and $NaKC_4H_4O_6$ to synthesize rugby-type $MnCO_3$ particles as precursors. Next, $Na_2Mn_3O_7$ (NMO) was obtained by calcining $MnCO_3$ and $NaNO_3$ with a molar ratio of 3:2 at 600 °C for 4 h. Finally, N was introduced into NMO via further calcination under an ammonia atmosphere. Sun et al. reported that sulfur-doped MnO_2 (S-MnO_2) nanosheets were obtained using a two-zone furnace for application as a high-performance cathode [57]. The S powder was placed on the upstream side under a temperature of 450 °C, while MnO_2 was placed on the downstream side under a temperature of 250 °C. This process was maintained for 1 h under Ar atmosphere.

3. Optimization Mechanism of Ion Doping in Zinc–Manganese Battery

Ion doping alters the behavior of electrode materials in a variety of ways. It is vital to produce a complete overview to develop better electrode materials and identify knowledge gaps for in-depth research in the future. As far as the current research progress is concerned, the positive effects of ion doping can be roughly divided into three categories: (1) enlarged interlayer spacing for improved ion diffusion kinetics, (2) defect engineering for enhanced electrical conductivity, and (3) pillar effect for enhanced stability of the host structure.

3.1. Enlarged Interlayer Spacing for Improved Ion Diffusion Kinetics

Theoretically, Zn^{2+} ions have a small ionic radius (0.74 Å) and high ionic conductivity in aqueous solution (~1–10 $mS·cm^{-1}$) [58]; however, in practice, due to their high charge density, Zn^{2+} ions combine with water molecules to form hydrated $[Zn(H_2O)_6]^{2+}$, leading to an increment in ionic radius to 5.5 Å, slowing down the diffusion of Zn^{2+}. Furthermore, the solid electrostatic effect between Zn^{2+} and the host structure of the cathode material also causes sluggish Zn^{2+} intercalation [59][60]. The diffusion rate of carriers has a linear negative relationship with the electrostatic repulsion (f) between the carriers and the host structure. According to the formula f∝1εrr20, where εr is the permittivity and r_0 is the distance between Zn^{2+} and the closest ions, a larger value of r_0 means faster diffusion kinetics [21][61]. In other words, a larger layer spacing leads to better diffusion dynamics. Ion doping is an efficient strategy to expand the layer spacing of the cathode material, thus enhancing performance.

Kim et al. reported that V-doped MnO_2 (VMO) could enhance zinc storage properties by expanding the layer spacing [62]. The (211) peak in the X-ray diffraction (XRD) patterns of VMO showed a minor shift toward lower scanning angles, as shown in **Figure 3**a, confirming anisotropy of the unit cell parameters, which would facilitate the insertion of zinc ions. Lu's group obtained a cathode with a larger interlamellar spacing by doping La^{3+} into δ-MnO_2 (LMO), which showed lower resistance of Zn^{2+} (de)insertion and better structural stability [63]. The rate performance of LMO was significantly improved (121.8 $mAh·g^{-1}$ at 1.6 $A·g^{-1}$) compared to pristine δ-MnO_2 (only 3.4 $mAh·g^{-1}$ at 1.6 $A·g^{-1}$). Zheng et al. reported that phosphate ion-doped MnO_2 could expand the interlayer spacing of the (001) plane from 0.68 nm to 0.70 nm, accelerating ion transfer. Simultaneously, oxygen vacancies were introduced via phosphorization, enhancing the electrical conductivity of MnO_2 [64]. Wang's work revealed that the pre-intercalation of Bi^{3+} into α-MnO_2 could effectively enlarge the lattice spacing and have a positive effect on the ion diffusion rates, resulting in a superior rate performance with a capacity retention of 150 $mAh·g^{-1}$ at 5 $A·g^{-1}$ [42]. $K_{0.29}MnO_2·0.67H_2O$ (KMO) with an interplanar spacing of 7.4 Å was synthesized via a simple hydrothermal strategy by Shi et al. [37], as shown in **Figure 3**b, exhibiting high capacity (300 $mAh·g^{-1}$ at 0.2 $A·g^{-1}$) and an ultralong cycle performance (158 $mAh·g^{-1}$ after 12,000 cycles at 2 $A·g^{-1}$). According to the XRD pattern in **Figure 3**c, this work calculated that the interlayer spacing corresponding to the (001) plane increased from 6.8 Å to 7.4 Å according to Bragg's rule. The diffusion energy barriers of H and Zn^{+2+} in MnO_2 and KMO were explored using density functional theory (DFT)-based first-principles calculations, and the results revealed a lower value of KMO (0.11 eV and 0.19 eV) than MnO_2 (0.32 eV and 0.49 eV), as shown in **Figure 3**d, indicating that the increased interlayer spacing indeed accelerated ion transfer. The kinetic behavior of the KMO sample was further investigated using the galvanostatic intermittence titration technique (GITT). As shown in **Figure 3**e,f, KMO displayed a smaller overpotential and higher diffusion coefficient than MnO_2 during the discharge process, which indicated that the doping of K indeed promoted ion diffusion kinetics.$^{+}$

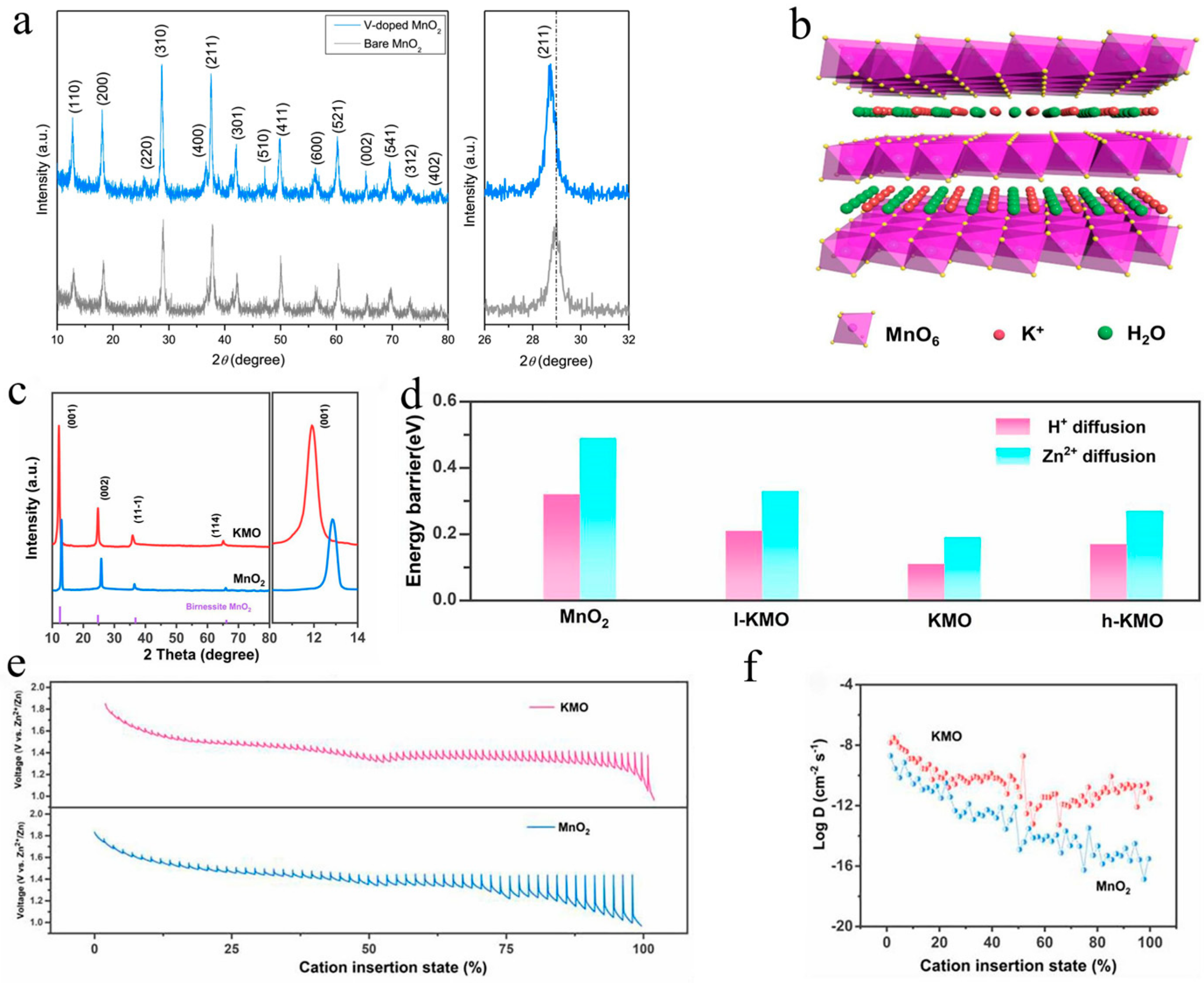

Figure 3. Enlarged interlayer spacing and faster ion diffusion kinetics: (**a**) XRD patterns of V-doped MnO_2 [62]; (**b**) structure schematic of KMO [37]; (**c**) XRD patterns of KMO and MnO_2 [37]; (**d**) calculation results of H and Zn^{+2+} diffusion energy barriers for KMO and MnO_2 electrodes using DFT [37]; (**e**) GITT image of KMO and MnO_2 electrodes [37]; (**f**) results of ion diffusion coefficients for KMO and MnO_2 electrodes [37].

3.2. Defect Engineering for Enhanced Electrical Conductivity

For secondary batteries, electron transfer between the cathode and anode is an integral part of completing the whole electrochemical reaction; hence, the electrical conductivity of the cathode plays an important role in the electrochemical performance [65]. However, manganese-based oxides are usually semiconductors with poor electrical conductivity [66]. The strategy of complexing with conductive agents is generally adopted to accelerate electron transfer, while ion doping is another method to enhance the electronic conductivity of cathode materials [67]. For example, a distinctive N-doped MnO_{2-x} cathode with numerous oxygen defects was prepared through NH_3 treatment at 200 °C by Xia et al. in 2019 [55]. Oxygen vacancies were introduced at the same time as N doping, which increased the electron density and lowered the bandgap of manganese dioxide, resulting in a better electronic conductivity and activity. As shown in **Figure 4**a, the position of the absorption edge corresponding to the oxidation of N-doped MnO_{2-x} in the XANES spectrum presented a shift toward a lower energy, indicating higher average electron density. On the other hand, the FT spectrum implied that N-doped MnO_2 did not change phase but increased its level of disorder. The DFT calculation results (**Figure 4**b) showed that N-doped MnO_{2-x} possessed a much smaller bandgap (0.12 eV) than pure MnO_2 (1.83 eV), revealing a significant enhancement of electronic conductivity. Excellent electrochemical performance was achieved that 285 $mAh·g^{-1}$ at 0.2 $A·g^{-1}$ with 85.7% retention after 1000 cycles at 1 $A·g^{-1}$. In the same year, Ti–MnO_2 with oxygen vacancies was reported by Mai's group [68], indicating that the replacement of manganese with titanium and the introduction of oxygen vacancies could break through the manganese–oxygen octahedral walls, resulting in heterogeneous charge distribution. As revealed by the EIS spectrum (**Figure 4**c), Ti-doped MnO_2 exhibited lower charge migration resistance, confirming that the unbalanced local electric field in the host structure could boost the mobility of ions/electrons. Furthermore, according to the DFT calculations (**Figure 4**d), the electron cloud of Ti substitution and its derived oxygen vacancies could balance the disordered interfacial electric field, allowing electron transit through the [MnO_6] octahedral walls. Liang et al. proposed a K-stabilized Mn-based cathode with rich oxygen defects ($K^+_{0.8}Mn_8O_{16}$ with oxygen defects), which exhibited impressive stability over 1000 cycles with no obvious fading [69]. As described in **Figure 4**d,e, oxygen defects could accelerate H diffusion by opening the [MnO^+_6] octahedral walls from the *ab*-plane. Moreover, the oxygen defects could reduce the energy for electron and charge transfer during the redox reaction, as illustrated in **Figure 4**e, KMO showed smaller overpotential gaps than pure MnO_2 (1.399/1.614 V vs. 1.389/1.612 V). More recently, Zhang et al. designed a cathode (O_{cu}–Mn_2O_3) by replacing sites of trivalent manganese with divalent copper ions to create oxygen defects in Mn_2O_3 for better electronic conductivity [70]. Long et al. fabricated a low-bandgap cathode ($Ni_xMn_{3-x}O_4$) via the replacement of Mn with Ni. The DOS indicated that Ni-doped Mn_3O_4 exhibited a narrower bandgap than pure Mn_3O_4 (1.20 eV), thereby significantly enhancing the electronic conductivity [53].

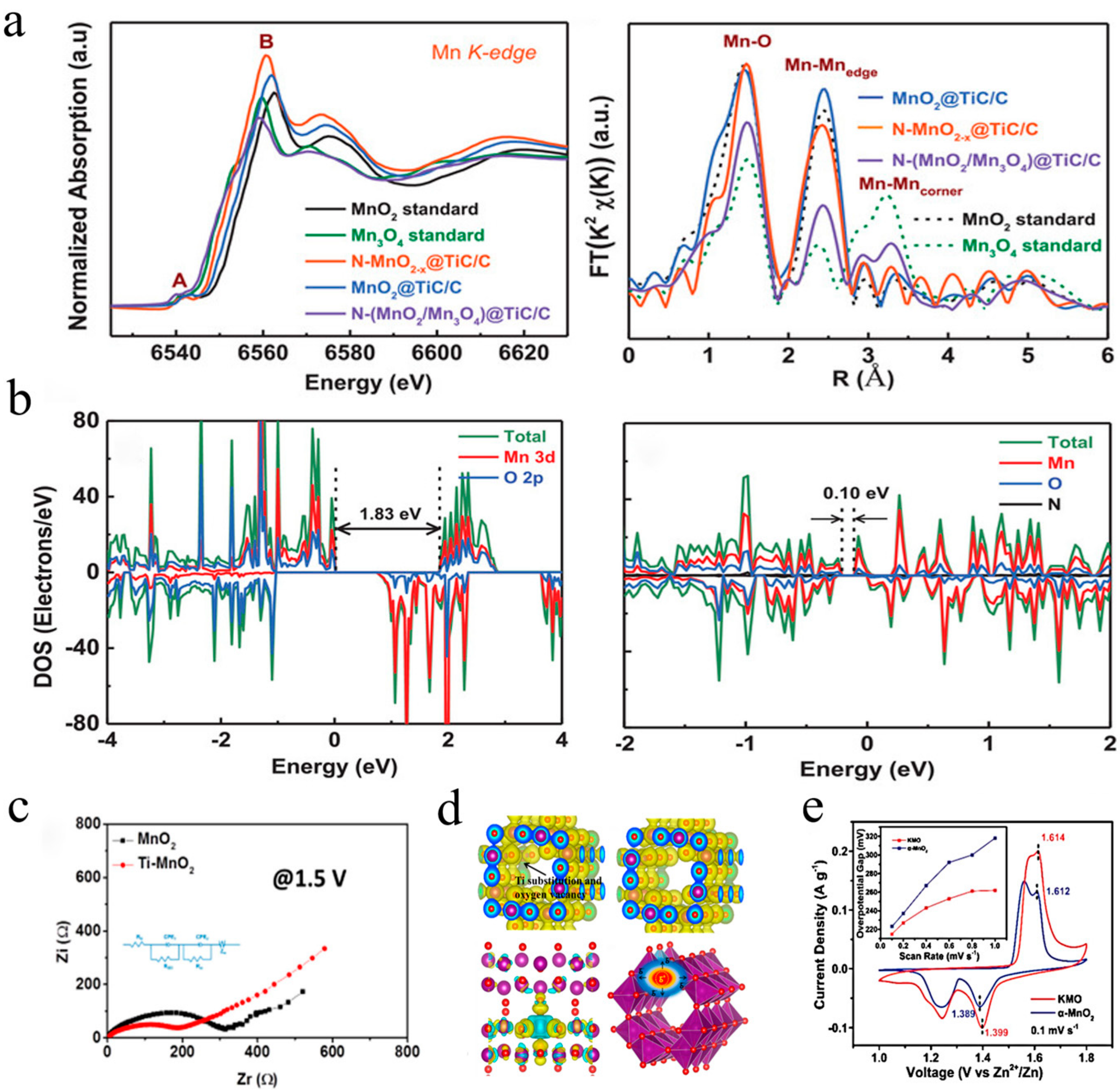

Figure 4. Defect engineering for improved electrical conductivity: (**a**) XANES and FT spectra of N–$MnO_{2−x}$ and MnO_2 [55]; (**b**) density of states results of MnO_2 and N–$MnO_{2−x}$ [55]; (**c**) schematic illustration of charge density differences and charge transfer behavior in Ti–MnO_2 and MnO_2 electrodes [68]; (**d**) GITT profile of Ti–MnO_2 and MnO_2 electrodes; (**e**) CV curves of KMO and α-MnO_2 [69].

References

1. Chu, S.; Majumdar, A. Opportunities and challenges for a sustainable energy future. Nature 2012, 488, 294–303.

2. Hosenuzzaman, M.; Rahim, N.A.; Selvaraj, J.; Hasanuzzaman, M.; Malek, A.B.M.A.; Nahar, A. Global prospects, progress, policies, and environmental impact of solar photovoltaic power generation. Renew. Sustain. Energy Rev. 2015, 41, 284–297.
3. Meng, J.; Guo, H.; Niu, C.; Zhao, Y.; Xu, L.; Li, Q.; Mai, L. Advances in structure and property optimizations of battery electrode materials. Joule 2017, 1, 522–547.
4. Sterl, S.; Vanderkelen, I.; Chawanda, C.J.; Russo, D.; Brecha, R.J.; van Griensven, A.; van Lipzig, N.P.M.; Thiery, W. Smart renewable electricity portfolios in West Africa. Nat. Sustain. 2020, 3, 710–719.
5. Larcher, D.; Tarascon, J.M. Towards greener and more sustainable batteries for electrical energy storage. Nat. Chem. 2015, 7, 19–29.
6. Tang, B.; Shan, L.; Liang, S.; Zhou, J. Issues and opportunities facing aqueous zinc-ion batteries. Energy Environ. Sci. 2019, 12, 3288–3304.
7. Blanc, L.E.; Kundu, D.; Nazar, L.F. Scientific challenges for the implementation of Zn-ion batteries. Joule 2020, 4, 771–799.
8. Goodenough, J.B.; Park, K.S. The Li-ion rechargeable battery: A perspective. J. Am. Chem. Soc. 2013, 135, 1167–1176.
9. Cao, Y.; Li, M.; Lu, J.; Liu, J.; Amine, K. Bridging the academic and industrial metrics for next-generation practical batteries. Nat. Nanotechnol. 2019, 14, 200–207.
10. Liu, T.; Dai, A.; Lu, J.; Yuan, Y.; Xiao, Y.; Yu, L.; Li, M.; Gim, J.; Ma, L.; Liu, J.; et al. Correlation between manganese dissolution and dynamic phase stability in spinel-based lithium-ion battery. Nat. Commun. 2019, 10, 4721.
11. Zhao, K.; Sun, C.; Yu, Y.; Dong, Y.; Zhang, C.; Wang, C.; Voyles, P.M.; Mai, L.; Wang, X. Surface gradient Ti-doped MnO2 nanowires for high-rate and long-life lithium battery. ACS Appl. Mater. Interfaces 2018, 10, 44376–44384.
12. Evarts, E.C. Lithium batteries: To the limits of lithium. Nature 2015, 526, S93–S95.
13. Chen, L.; An, Q.; Mai, L. Recent advances and prospects of cathode materials for rechargeable aqueous zinc-ion batteries. Adv. Mater. Interfaces 2019, 6, 1900387.
14. Huang, J.; Guo, Z.; Ma, Y.; Bin, D.; Wang, Y.; Xia, Y. Recent progress of rechargeable batteries using mild aqueous electrolytes. Small Methods 2019, 3, 1800272.
15. Chao, D.; Zhou, W.; Xie, F.; Ye, C.; Li, H.; Jaroniec, M.; Qiao, S.Z. Roadmap for advanced aqueous batteries: From design of materials to applications. Sci. Adv. 2020, 6, eaba4098.
16. Xiong, F.; Jiang, Y.; Cheng, L.; Yu, R.; Tan, S.; Tang, C.; Zuo, C.; An, Q.; Zhao, Y.; Gaumet, J.J. Low-strain TiP2O7 with three-dimensional ion channels as long-life and high-rate anode material

for Mg-ion batteries. Interdiscip. Mater. 2022, 1, 140–147.

17. Li, C.; Xie, X.; Liang, S.; Zhou, J. Issues and future perspective on zinc metal anode for rechargeable aqueous zinc-ion batteries. Energy Environ. Mater. 2020, 3, 146–159.
18. Shin, J.; Lee, J.; Park, Y.; Choi, J.W. Aqueous zinc ion batteries: Focus on zinc metal anodes. Chem. Sci. 2020, 11, 2028–2044.
19. Huang, S.; Zhu, J.; Tian, J.; Niu, Z. Recent progress in the electrolytes of aqueous zinc-ion batteries. Chem. Eur. J. 2019, 25, 14480–14494.
20. Shi, W.; Lee, W.S.V.; Xue, J. Recent development of Mn-based oxides as zinc-ion battery cathode. ChemSusChem 2021, 14, 1634–1658.
21. Zhao, Q.; Song, A.; Ding, S.; Qin, R.; Cui, Y.; Li, S.; Pan, F. Preintercalation strategy in manganese oxides for electrochemical energy storage: Review and prospects. Adv. Mater. 2020, 32, e2002450.
22. Ming, J.; Guo, J.; Xia, C.; Wang, W.; Alshareef, H.N. Zinc-ion batteries: Materials, mechanisms, and applications. Mater. Sci. Eng. R Rep. 2019, 135, 58–84.
23. Yu, P.; Zeng, Y.; Zhang, H.; Yu, M.; Tong, Y.; Lu, X. Flexible Zn-ion batteries: Recent progresses and challenges. Small 2019, 15, e1804760.
24. Zhou, L.; Zhuang, Z.; Zhao, H.; Lin, M.; Zhao, D.; Mai, L. Intricate Hollow Structures: Controlled Synthesis and Applications in Energy Storage and Conversion. Adv. Mater. 2017, 29, 1602914.
25. Guo, C.; Liu, H.; Li, J.; Hou, Z.; Liang, J.; Zhou, J.; Zhu, Y.; Qian, Y. Ultrathin δ-MnO2 nanosheets as cathode for aqueous rechargeable zinc ion battery. Electrochim. Acta 2019, 304, 370–377.
26. Wang, J.; Wang, J.G.; Qin, X.; Wang, Y.; You, Z.; Liu, H.; Shao, M. Superfine MnO2 nanowires with rich defects toward boosted zinc ion storage performance. ACS Appl Mater. Interfaces 2020, 12, 34949–34958.
27. Baral, A.; Satish, L.; Zhang, G.; Ju, S.; Ghosh, M.K. A review of recent progress on nano MnO2: Synthesis, surface modification and applications. J. Inorg. Organomet. Polym Mater. 2020, 31, 899–922.
28. Xiong, T.; Zhang, Y.; Lee, W.S.V.; Xue, J. Defect engineering in manganese-based oxides for aqueous rechargeable zinc-ion batteries: A review. Adv. Energy Mater. 2020, 10, 2001769.
29. Xu, W.W.; Sun, C.L.; Wang, N.; Liao, X.B.; Zhao, K.N.; Yao, G.; Sun, Q.C.; Cheng, H.W.; Wang, Y.; Lu, X.G. Sn stabilized pyrovanadate structure rearrangement for zinc ion battery. Nano Energy 2021, 81, 105584.
30. Yao, X.; Zhao, Y.; Castro, F.A.; Mai, L. Rational design of preintercalated electrodes for rechargeable batteries. ACS Energy Lett. 2019, 4, 771–778.

31. Kitchaev, D.A.; Dacek, S.T.; Sun, W.; Ceder, G. Thermodynamics of phase selection in MnO2 framework structures through alkali intercalation and hydration. J. Am. Chem. Soc. 2017, 139, 2672–2681.

32. Hu, X.; Kitchaev, D.A.; Wu, L.; Zhang, B.; Meng, Q.; Poyraz, A.S.; Marschilok, A.C.; Takeuchi, E.S.; Takeuchi, K.J.; Ceder, G. Revealing and rationalizing the rich polytypism of todorokite MnO2. J. Am. Chem. Soc. 2018, 140, 6961–6968.

33. Peng, X.; Peng, H.; Zhao, K.; Zhang, Y.; Xia, F.; Lyu, J.; Van Tendeloo, G.; Sun, C.; Wu, J. Direct visualization of atomic-scale heterogeneous structure dynamics in MnO2 nanowires. ACS Appl. Mater. Interfaces 2021, 13, 33644–33651.

34. Liu, G.; Huang, H.; Bi, R.; Xiao, X.; Ma, T.; Zhang, L. K+ pre-intercalated manganese dioxide with enhanced Zn2+ diffusion for high rate and durable aqueous zinc-ion batteries. J. Mater. Chem. A 2019, 7, 20806–20812.

35. Zhao, Q.H.; Chen, X.; Yang, L.Y.; Chen, H.B.; Pan, F. Unravelling H+/Zn2+ synergistic intercalation in a novel phase of manganese oxide for high-performance aqueous rechargeable battery. Small 2019, 15, 1904545.

36. Ding, S.; Liu, L.; Qin, R.; Chen, X.; Song, A.; Li, J.; Li, S.; Zhao, Q.; Pan, F. Progressive “layer to hybrid spinel/layer” phase evolution with proton and Zn2+ co-intercalation to enable high performance of MnO2-based aqueous batteries. ACS Appl. Mater. Interfaces 2021, 13, 22466–22474.

37. Wang, D.; Zhang, S.; Li, C.; Chen, X.; Wang, W.; Han, Y.; Lin, H.; Shi, Z.; Feng, S. Engineering the interplanar spacing of K-birnessite for ultra-long cycle Zn-ion battery through “hydrothermal potassium insertion” strategy. Chem. Eng. J. 2022, 435, 134754.

38. Peng, H.; Fan, H.; Yang, C.; Tian, Y.; Wang, C.; Sui, J. Ultrathin δ-MnO2 nanoflakes with Na+ intercalation as a high-capacity cathode for aqueous zinc-ion batteries. RSC Adv. 2020, 10, 17702–17712.

39. Sun, T.; Nian, Q.; Zheng, S.; Shi, J.; Tao, Z. Layered Ca0. 28MnO2·0.5H2O as a high performance cathode for aqueous zinc-Ion battery. Small 2020, 16, 2000597.

40. Zhao, Q.; Song, A.; Zhao, W.; Qin, R.; Ding, S.; Chen, X.; Song, Y.; Yang, L.; Lin, H.; Li, S.; et al. Boosting the energy density of aqueous batteries via facile grotthuss proton transport. Angew. Chem. Int. Ed. Engl. 2021, 60, 4169–4174.

41. Wang, J.; Sun, X.; Zhao, H.; Xu, L.; Xia, J.; Luo, M.; Yang, Y.; Du, Y. Superior-performance aqueous zinc ion battery based on structural transformation of MnO2 by rare earth doping. J. Mater. Chem. C 2019, 123, 22735–22741.

42. Ma, K.; Li, Q.; Hong, C.; Yang, G.; Wang, C. Bi doping-enhanced reversible-phase transition of alpha-MnO2 raising the cycle capability of aqueous Zn-Mn batteries. ACS Appl. Mater. Interfaces

2021, 13, 55208–55217.

43. Chen, C.; Shi, M.; Zhao, Y.; Yang, C.; Zhao, L.; Yan, C. Al-intercalated MnO2 cathode with reversible phase transition for aqueous Zn-ion batteries. Chem. Eng. J. 2021, 422, 130375.
44. Xu, J.; Hu, X.; Alam, M.A.; Muhammad, G.; Lv, Y.; Wang, M.; Zhu, C.; Xiong, W. Al-doped α-MnO2 coated by lignin for high-performance rechargeable aqueous zinc-ion batteries. RSC Adv. 2021, 11, 35280–35286.
45. Zhong, Y.; Xu, X.; Veder, J.P.; Shao, Z. Self-recovery chemistry and cobalt-catalyzed electrochemical deposition of cathode for boosting performance of aqueous zinc-Ion batteries. iScience 2020, 23, 100943.
46. Wu, Y.; Wang, M.; Tao, Y.; Zhang, K.; Cai, M.; Ding, Y.; Liu, X.; Hayat, T.; Alsaedi, A.; Dai, S. Electrochemically derived graphene-like carbon film as a superb substrate for high-performance aqueous Zn-ion batteries. Adv. Funct. Mater. 2020, 30, 1907120.
47. Zhang, D.; Cao, J.; Zhang, X.; Insin, N.; Wang, S.; Han, J.; Zhao, Y.; Qin, J.; Huang, Y. Inhibition of manganese dissolution in Mn2O3 cathode with controllable Ni2+ incorporation for high-performance zinc ion battery. Adv. Funct. Mater. 2021, 31, 2009412.
48. Sun, M.; Li, D.S.; Wang, Y.F.; Liu, W.L.; Ren, M.M.; Kong, F.G.; Wang, S.J.; Guo, Y.Z.; Liu, Y.M. Mn3O4@NC composite nanorods as a cathode for rechargeable aqueous Zn-ion batteries. ChemElectroChem 2019, 6, 2510–2516.
49. Wu, Y.; Zhang, K.; Chen, S.; Liu, Y.; Tao, Y.; Zhang, X.; Ding, Y.; Dai, S. Proton inserted manganese dioxides as a reversible cathode for aqueous Zn-ion batteries. ACS Appl. Energy Mater. 2019, 3, 319–327.
50. Yadav, G.G.; Gallaway, J.W.; Turney, D.E.; Nyce, M.; Huang, J.; Wei, X.; Banerjee, S. Regenerable Cu-intercalated MnO2 layered cathode for highly cyclable energy dense batteries. Nat. Commun. 2017, 8, 14424.
51. Kataoka, F.; Ishida, T.; Nagita, K.; Kumbhar, V.; Yamabuki, K.; Nakayama, M. Cobalt-doped layered MnO2 thin film electrochemically grown on nitrogen-doped carbon cloth for aqueous zinc-ion batteries. ACS Appl. Energy Mater. 2020, 3, 4720–4726.
52. Ji, J.; Wan, H.; Zhang, B.; Wang, C.; Gan, Y.; Tan, Q.; Wang, N.; Yao, J.; Zheng, Z.; Liang, P.; et al. Co2+/3+/4+-regulated electron state of Mn-O for superb aqueous zinc-manganese oxide batteries. Adv. Energy Mater. 2020, 11, 2003203.
53. Long, J.; Gu, J.; Yang, Z.; Mao, J.; Hao, J.; Chen, Z.; Guo, Z. Highly porous, low band-gap NixMn3−xO4 (0.55 ≤ x ≤ 1.2) spinel nanoparticles with in situ coated carbon as advanced cathode materials for zinc-ion batteries. J. Mater. Chem. A 2019, 7, 17854–17866.

54. Fu, Y.; Wei, Q.; Zhang, G.; Wang, X.; Zhang, J.; Hu, Y.; Wang, D.; Zuin, L.; Zhou, T.; Wu, Y. High-performance reversible aqueous Zn-ion battery based on porous MnOx nanorods coated by MOF-derived N-doped carbon. Adv. Energy Mater. 2018, 8, 1801445.
55. Zhang, Y.; Deng, S.; Luo, M.; Pan, G.; Zeng, Y.; Lu, X.; Ai, C.; Liu, Q.; Xiong, Q.; Wang, X.; et al. Defect promoted capacity and durability of N-MnO2-x branch arrays via low-temperature NH3 treatment for advanced aqueous zinc ion batteries. Small 2019, 15, e1905452.
56. Cheng, X.; Xiao, J.; Ye, M.; Zhang, Y.; Yang, Y.; Li, C.C. Achieving stable zinc-ion storage performance of manganese oxides by synergistic engineering of the interlayer structure and interface. ACS Appl. Mater. Interfaces 2022, 14, 10489–10497.
57. Zhao, Y.; Zhang, P.; Liang, J.; Xia, X.; Ren, L.; Song, L.; Liu, W.; Sun, X. Uncovering sulfur doping effect in MnO2 nanosheets as an efficient cathode for aqueous zinc ion battery. Energy Storage Mater. 2022, 47, 424–433.
58. Li, J.; McColl, K.; Lu, X.; Sathasivam, S.; Dong, H.; Kang, L.; Li, Z.; Zhao, S.; Kafizas, A.G.; Wang, R.; et al. Multi-scale investigations of δ-Ni0.25V2O5·nH2O cathode materials in aqueous zinc-ion batteries. Adv. Energy Mater. 2020, 10, 2000058.
59. Kundu, D.; Hosseini Vajargah, S.; Wan, L.; Adams, B.; Prendergast, D.; Nazar, L.F. Aqueous vs. nonaqueous Zn-ion batteries: Consequences of the desolvation penalty at the interface. Energy Environ. Sci. 2018, 11, 881–892.
60. Liu, Y.; He, G.; Jiang, H.; Parkin, I.P.; Shearing, P.R.; Brett, D.J.L. Cathode design for aqueous rechargeable multivalent ion batteries: Challenges and opportunities. Adv. Funct. Mater. 2021, 31, 2010445.
61. Yan, M.; He, P.; Chen, Y.; Wang, S.; Wei, Q.; Zhao, K.; Xu, X.; An, Q.; Shuang, Y.; Shao, Y. Water-lubricated intercalation in V2O5·nH2O for high-capacity and high-rate aqueous rechargeable zinc batteries. Adv. Mater. 2018, 30, 1703725.
62. Alfaruqi, M.H.; Islam, S.; Mathew, V.; Song, J.; Kim, S.; Tung, D.P.; Jo, J.; Kim, S.; Baboo, J.P.; Xiu, Z.; et al. Ambient redox synthesis of vanadium-doped manganese dioxide nanoparticles and their enhanced zinc storage properties. Appl. Surf. Sci. 2017, 404, 435–442.
63. Zhang, H.; Liu, Q.; Wang, J.; Chen, K.; Xue, D.; Liu, J.; Lu, X. Boosting the Zn-ion storage capability of birnessite manganese oxide nanoflorets by La3+ intercalation. J. Mater. Chem. A 2019, 7, 22079–22083.
64. Zhang, Y.; Deng, S.; Pan, G.; Zhang, H.; Liu, B.; Wang, X.L.; Zheng, X.; Liu, Q.; Wang, X.; Xia, X.; et al. Introducing oxygen defects into phosphate ions intercalated manganese dioxide/vertical multilayer graphene arrays to boost flexible zinc ion storage. Small Methods 2020, 4, 1900828.
65. Zheng, J.; Ye, Y.; Pan, F. ‘Structure units’ as material genes in cathode materials for lithium-ion batteries. Natl. Sci. Rev. 2020, 7, 242–245.

66. Young, M.J.; Holder, A.M.; George, S.M.; Musgrave, C.B. Charge storage in cation incorporated α-MnO2. Chem. Mater. 2015, 27, 1172–1180.

67. Jia, X.; Liu, C.; Neale, Z.G.; Yang, J.; Cao, G. Active materials for aqueous zinc ion batteries: Synthesis, crystal structure, morphology, and electrochemistry. Chem. Rev. 2020, 120, 7795–7866.

68. Lian, S.; Sun, C.; Xu, W.; Huo, W.; Luo, Y.; Zhao, K.; Yao, G.; Xu, W.; Zhang, Y.; Li, Z.; et al. Built-in oriented electric field facilitating durable Zn MnO2 battery. Nano Energy 2019, 62, 79–84.

69. Fang, G.; Zhu, C.; Chen, M.; Zhou, J.; Tang, B.; Cao, X.; Zheng, X.; Pan, A.; Liang, S. Suppressing manganese dissolution in potassium manganate with rich oxygen defects engaged high-energy-density and durable aqueous zinc-ion battery. Adv. Funct. Mater. 2019, 29, 1808375.

70. Liu, N.; Wu, X.; Yin, Y.; Chen, A.; Zhao, C.; Guo, Z.; Fan, L.; Zhang, N. Constructing the efficient ion diffusion pathway by introducing oxygen defects in Mn2O3 for high-performance aqueous zinc-ion batteries. ACS Appl Mater. Interfaces 2020, 12, 28199–28205.

Retrieved from https://encyclopedia.pub/entry/history/show/60526